

Cepheid metallicity in the Leavitt law (C-MetaLL) survey – III. Simultaneous derivation of the *Gaia* parallax offset and Period-Luminosity-Metallicity coefficients.

R. Molinaro^{1*}, V. Ripepi¹, M. Marconi¹, M. Romaniello², G. Catanzaro³, F. Cusano⁴, G. De Somma^{1,5}, I. Musella¹, J. Storm⁶, E. Trentin^{1,6,7}

¹INAF-OACN Osservatorio Astronomico di Capodimonte, salita Moiariello 16, Napoli (ITALY)

²European Southern Observatory (ESO), Karl-Schwarzschild-Str., D-85748 Garching, Germany

³INAF-Osservatorio Astrofisico di Catania, via Santa Sofia 78, 95125, Catania, Italy

⁴INAF-Osservatorio di Astrofisica e Scienza dello Spazio, Via Gobetti 93/3, I-40129 Bologna, Italy

⁵Istituto Nazionale di Fisica Nucleare (INFN)-Sez. di Napoli, via Cinthia 80126 Napoli, Italy

⁶Leibniz Institut für Astrophysik Potsdam (AIP), An der Sternwarte 16, D-14482 Potsdam, Germany

⁷Institut für Physik und Astronomie, Univ. Potsdam, Karl-Liebknecht-Strasse 24/25, D-14476 Potsdam, Germany

Accepted XXX. Received YYY; in original form ZZZ

ABSTRACT

Classical Cepheids (DCEPs) are the most important standard candles in the extra-galactic distance scale thanks to the Period-Luminosity (PL), Period-Luminosity-Color (PLC) and Period-Wesenheit (PW) relations that hold for these objects. The advent of the *Gaia* mission, and in particular the Early Data Release 3 (EDR3) provided accurate parallaxes to calibrate these relations. In order to fully exploit *Gaia* measurements, the zero point (ZP) of *Gaia* parallaxes should be determined with an accuracy of a few μas . The individual ZP corrections provided by the *Gaia* team depend on the magnitude and the position on the sky of the target. In this paper, we use an implicit method that relies on the Cepheid PL and PW relations to evaluate the ensemble *Gaia* parallax zero point. The best inferred estimation of the offset value needed to additionally correct (after the *Gaia* team correction) the *Gaia* parallaxes of the present DCEP sample, amounts to $-22 \pm 4 \mu\text{as}$. This value is in agreement with the most recent literature values and confirms that the correction proposed by the *Gaia* team over-corrected the parallaxes.

As a further application of our results, we derive an estimate of the Large Magellanic Cloud distance ($\mu_0 = 18.49 \pm 0.06 \text{ mag}$), in very good agreement with the currently accepted value obtained through geometric methods.

Key words: Stars: distances — Stars: variables: Cepheids — (cosmology:) distance scale < Cosmology – surveys < Astronomical Data bases

1 INTRODUCTION

Classical Cepheids (DCEPs) are young (50-500 Myr) stellar pulsators crossing the instability strip during the central helium-burning phase. They are the most important standard candles in the extra-galactic distance scale thanks to their Period-Luminosity (PL), Period-Luminosity-Color (PLC) and Period-Wesenheit (PW) relations (e.g. Leavitt & Pickering 1912; Madore 1982; Caputo, Marconi, & Musella 2000; Riess et al. 2016). Indeed, these relations allow us to calibrate the secondary distance indicators such as Supernovae Ia, and eventually, to estimate the value of the Hubble constant (H_0) (e.g. Riess et al. 2016). However, it is now well known (e.g. Riess et al. 2022, and references therein) that there exists a discrepancy at the level of 5σ between the value of H_0 as measured with the Cepheid-based and SNIa-based extra-galactic distance scale and that estimated from the early universe from the cosmic microwave background and the Λ CDM (Cold Dark Matter) theory (Planck Collaboration et al. 2020). In spite of many observational and theoretical

efforts, the causes of this discrepancy are still unknown. In this context, it is important to investigate in detail all the possible causes of systematic errors in the methods adopted to estimate H_0 . Concerning the cosmic distance scale, one of the possible sources of systematic error is the dependence of PL, PLC and PW relations on metallicity, which is still not well constrained (see Anderson et al. 2016; Gieren et al. 2018; Groenewegen 2018; Ripepi et al. 2019; Breuval et al. 2021, 2022; Riess et al. 2021, 2022; Ripepi et al. 2021; De Somma et al. 2022; Ripepi et al. 2022; Trentin et al. 2022). To tackle this problem, we started a project dubbed C-MetaLL (Cepheids - Metallicity in the Leavitt Law, see Ripepi et al. (2021, hereafter R21) for full details on the project) with the aim of obtaining new high-resolution spectroscopy and homogeneous photometry both in the optical and in the near-infrared (NIR) for a significant sample (i.e. > 250 objects) of DCEPs spanning a wide range of metallicity values (e.g. $-1.0 < [\text{Fe}/\text{H}] < +0.5$). These data, in conjunction with the parallaxes from the *Gaia* mission (Gaia Collaboration et al. 2016) will allow us to derive accurate PLZ and PWZ relations (Z stands for metallicity).

* E-mail: roberto.molinaro@inaf.it

However, it is well known that *Gaia* parallaxes are affected by an

offset and their values need to be corrected before any scientific use (Gaia Collaboration et al. 2018; Luri et al. 2018). This offset, found by studying the parallax values for a sample of half a million quasars, assumed to have zero parallax, was found to depend on both the colour and the magnitude of the source, as well as on its position in the sky. In the Data Release 2 (DR2), the offset was found to be at least 29 μas or larger (see e.g. Arenou et al. 2018; Lindegren et al. 2018; Leung & Bovy 2019; Ripepi et al. 2020). The publication of Early Data Release 3 (EDR3 Gaia Collaboration et al. 2021) was accompanied by a recipe to calculate the individual offset values to be used for each star, depending on its ecliptic latitude, magnitude and colour (Lindegren et al. 2021, hereafter L21). However, subsequent studies found that the L21 method actually over-corrected the EDR3 parallaxes, with the need for an additional offset to obtain accurate parallaxes (see e.g. Bhardwaj et al. 2021; Fabricius et al. 2021; Gilligan et al. 2021; Huang et al. 2021; Ren et al. 2021; Riess et al. 2021; Stassun & Torres 2021; Vasiliev & Baumgardt 2021; Zinn 2021; Cruz Reyes & Anderson 2022; Wang, Yuan, & Huang 2022).

In the first work of this series, R21 checked their PLZ relations, derived for various band combinations, against the accurate geometric distance of the (Large Magellanic Cloud) LMC (Pietrzyński et al. 2019). In their analysis the *Gaia* EDR3 parallaxes were corrected according to both the L21 recipe and including the offset determined by Riess et al. (2021), but no final conclusion was inferred about the parallax offset value. Anyway, they found an interesting correlation of the parallax shift value with the metallicity coefficient of the PLZ and PWZ relations. In particular they found that the two parameters are degenerate: the effect of changing the parallax offset can be mimicked by varying the metallicity term in the PLZ and PWZ relations.

In the context of the C-MetaLL program, this paper aims to simultaneously determine the PLZ coefficients and the *Gaia* parallax offset, by applying the fitting technique described in Layden et al. (2019) to a sample of RR Lyrae stars and successfully applied to EDR3 parallaxes by (Gilligan et al. 2021).

The paper is structured as follows: the fitting technique together with the Monte Carlo simulations are introduced in Sect. 2; the results of the applied fit, together with an application consisting in estimating the LMC distance are described in Sect. 3; a discussion including the comparison with recent literature results is contained in Sect. 4; finally Sect. 5 contains our conclusions.

2 THE FITTING PROCEDURE

Before describing the procedure adopted to obtain the PLZ and PWZ relations with the implicit method, we briefly illustrate the observational sample used in this work.

2.1 The observational sample

We adopted the DCEPs sample devised in R21, which is composed of 443 stars¹, subdivided in 358 fundamental, 63 first overtone and 22 multi-mode² pulsators (DCEP_F, DCEP_1O, and DCEP_MULTI, respectively). The catalogue includes the iron abundance ([Fe/H]) value based on high-resolution spectroscopy and photometry in the

V, I, J, H, K_s bands³. Periods are taken from the literature or re-determined in R21, while the parallaxes with relative errors are from the *Gaia* EDR3 catalogue.

2.2 The method

To preserve the Gaussian properties of the parallax errors and to avoid introducing biases by neglecting negative parallaxes, we adopted the Astrometric Based Luminosity (ABL) formalism (Feast & Catchpole 1997; Arenou & Luri 1999). Specifically, we can write the PLZ or PWZ relations as follows:

$$\text{ABL} = \varpi 10^{0.2m-2} = 10^{0.2(\alpha+(\beta+\delta[\text{Fe}/\text{H}])(\log P-\log P_0)+\gamma[\text{Fe}/\text{H}])} \quad (1)$$

where ϖ is the parallax, m is the observed dereddened apparent magnitude or the reddening free Wesenheit⁴ pseudo-magnitude (Madore 1982), P is the period (in days) and $[\text{Fe}/\text{H}]$ is the iron abundance. The pivot value $\log P_0$ is also considered in the equation to reduce the correlation among fitted coefficients.

The idea consists in fitting simultaneously the coefficients of equation 1 and the *Gaia* parallax offset. To this aim the equation 1 can be written using an implicit form and introducing the parallax offset as a further parameter of the fit (Layden et al. 2019):

$$f = 10^{0.2(\alpha+(\beta+\delta[\text{Fe}/\text{H}])(\log P-\log P_0)+\gamma[\text{Fe}/\text{H}])} - (\varpi+\epsilon) 10^{0.2m-2} = 0, \quad (2)$$

where ϵ represents the parallax offset.

To face the problem of solving this implicit equation, we have used the open-source FORTRAN package ODRPACK95 (Zwolak et al. 2007). This software (hereafter ODR) allows us to solve weighted fitting problems when errors have to be considered on all variables. In these cases, the software minimizes the orthogonal distance of the input data from the fitted line and/or surface. Moreover, it allows parameter estimation also in the case of implicit fit, as the one considered in this paper (Eq. 2). The base algorithm consists of the Levenberg-Marquardt method (Levenberg 1944; Marquardt 1963) and is also able to calculate the input function derivatives by using the finite difference method if the Jacobian matrix is not provided by the user (Zwolak et al. 2007; Boggs et al. 1989, and references therein). In our case, we provided both the fitted function and its Jacobian matrix, but we verified that the results do not change by using the internal derivative method.

According to Zwolak et al. (2007), fixing the weights when all variables are affected by errors, is not straightforward. The values of the weights should compensate for precision differences among the variables and their spread over intervals covering different orders of magnitudes. As a consequence, wrong weight values can affect the fit results providing unreliable coefficients. Therefore, we performed both the weighted and the unweighted analyses in order to verify if they return consistent results. Moreover, we first carried out a large set of Monte Carlo simulations to test how the fitting routine is

³ We included also the F555W, F814W and F160W Hubble Space Telescope (HST) bands obtained from ground based V, I, H bands by using the transformations by Breuval et al. (2020)

⁴ Given a generic photometric band X and a generic color Y-Z, the Wesenheit pseudo-magnitude is defined by $W(X, Y-Z) = X + \lambda \cdot (Y-Z)$, where the coefficient λ is equal to the total-to-selective extinction ratio $R_X = \frac{A_X}{E(Y-Z)}$. The obtained quantity is reddening-free by definition.

¹ After sample cleaning as detailed in R21

² For these objects we used the longest period of pulsation

| Bands | λ |
|-------------------------|-----------|
| $W_{V,V-K_s}$ | -0.690 |
| $W_{V,J-K_s}$ | -0.130 |
| $W_{H,V-I}$ | -0.461 |
| $W_{F160W,F555W-F814W}$ | -0.386 |

Table 1. The color term coefficients used to calculate the Wesenheit magnitudes considered in this work: the band combinations are listed in column 1, while the λ values, obtained by applying the Cardelli law (Cardelli, Clayton, & Mathis 1989), are in column 2.

able to recover the PLZ or PWZ coefficients, assuming known input relations.

In the following, we apply the whole procedure to the observational sample presented above, considering both the F-mode DCEPs only and the global F+1O DCEPs sample. In the latter case, the 1O pulsators' periods were fundamentalised according to the recipe by Feast & Catchpole (1997). The PLZ and PWZ relations are calculated for a variety of bands and colours, specifically: K_s , $W_{V,V-K_s}$, $W_{V,J-K_s}$, $W_{H,V-I}$ and $W_{H,V-I}^{\text{HST}}$ ⁵. To calculate the Wesenheit magnitudes we adopted the coefficients for the color terms listed in the Tab. 1.

2.3 Monte Carlo simulations

In this section we present the simulations performed to test how our mathematical procedure is able to recover the correct coefficients of the fitted equation. First, we introduce the procedure adopted to simulate observational data. Then, we describe the fitting cases considered in this work.

2.3.1 Procedure

Following a procedure similar to that described by Layden et al. (2019), we simulated 1000 samples containing the same number of stars as in the sample analyzed in this work. To simulate the observed quantities (i.e. magnitudes, [Fe/H] values and period of pulsation), we assumed that the observations reported by R21 are the characterizing parameters (mean and standard deviation) of Gaussian distributions. Then we randomly extracted the values of magnitudes, metallicity and period from the quoted distributions.

As for the distance, assuming a known PLZ or PWZ relations (hereafter PLZ_{true} , PWZ_{true}), we used the simulated data to calculate the absolute magnitude and then the 'true' parallax of all sources. In particular, given the pulsational period and the [Fe/H] values, the $PLZ_{\text{true}}/PWZ_{\text{true}}$ relation in the generic band X allows to calculate the absolute magnitude M_X as:

$$M_X = \alpha_X + (\beta_X + \delta_X [\text{Fe}/\text{H}]) \log P + \gamma_X [\text{Fe}/\text{H}] \quad (3)$$

where α_X , β_X , γ_X and δ_X , are taken from Ripepi et al. (2021) for all the band combinations considered in this work. The distance modulus is therefore given by $\mu_0 = m_0 - M_X$, where m_0 is the absorption corrected apparent magnitude, while the parallax is obtained by:

$$\varpi(\text{mas}) = 1000 \cdot 10^{-(1+0.2\mu_0)} \quad (4)$$

⁵ To transform Johnson-Cousins-2MASS ground-based H, V, I photometry into the HST correspondent F160W, F555W, F814W, we adopted the transformations provided by Breuval et al. (2020).

The observed parallax was then drawn randomly from the Gaussian distributions having as mean the 'true' parallax and as standard deviation the parallax error of the original sample. Finally, a given offset was added to the simulated parallaxes.

To test the effect of bad data points on the fit results, we have also simulated the presence of measurement outliers. Specifically, we substituted a randomly selected fraction of the full sample absolute magnitudes, with values drawn from a uniform distribution.

Every simulated sample was then processed by the ODR routine and the obtained parameters were compared with the coefficients of the input PLZ_{true} or of the PWZ_{true} and with the chosen parallax offset. The coefficients of the PLZ_{true} and of the PWZ_{true} relations were fixed according to the recent results by R21⁶, while the parallax offset was arbitrarily chosen to be equal to 10 μas , but we verified that the simulation results do not depend on the particular value of the offset.

To take into account the presence of the quoted outlier points we have performed a σ -clipping procedure by testing different values for the number of σ ($n_\sigma = 1.5, 2, 2.5, 3, 3.5, 4, 4.5, 5, 6, 7, 8, 9, 10, 15$) used to detect the bad data points. Two outlier estimators have been considered: one based on the Median Absolute Deviation (MAD) and the other on the Double Median Absolute Deviation (DMAD), both applied to the residuals around the fit⁷. Our first aim is to understand the effect, if any, of the chosen number of sigmas for MADs/DMADs (respectively n_{MAD} , n_{DMAD}) on the parameter estimation.

To quantify how much the parameters obtained from the 1000 simulations differ from the expected values, indicating with p the generic fitted coefficient, we calculated the quantity $\Delta(\%) = 100 \cdot \frac{p_{\text{fit}} - p_{\text{true}}}{p_{\text{fit}}}$. This provides an estimate of the systematic error performed by the adopted fitting routine. Together with the systematic error, we calculated also the statistical error (hereafter σ) by considering the robust standard deviation ($1.4826 \cdot \text{MAD}$) of the parameter distributions obtained by running the Monte Carlo simulations. The obtained systematic and statistical error values are listed in Table. 2.

Hereafter we analyse the results for the following cases considered in this work: i) all the coefficients of Eq. 2 have been fitted ($\alpha\beta\gamma\delta\epsilon$ -case); ii) the δ coefficient has not been fitted, but its dependence is present in the adopted PLZ_{true} and PWZ_{true} relations ($\alpha\beta\gamma\epsilon$ -case); iii) the δ coefficient has been neglected both by the fitting routine and in the adopted PLZ_{true} and PWZ_{true} relations ($\alpha\beta\gamma\epsilon$ -pure -case).

2.3.2 $\alpha\beta\gamma\delta\epsilon$ -case

The left panels of Fig.1, show the median of the Δ differences (Δ_s) as a function of n_{MAD} used for the outlier rejection. The results for the K_s , $W_{\text{HVI}}^{\text{HST}}$, W_{HVI} , W_{JK_s} and W_{VK_s} magnitudes are plotted from top to bottom, and in each panel different colors indicate different parameters. For clarity reason, here we show only the results for the MAD case, but for the DMAD we obtain similar conclusions. The right panels in Fig. 1 show the relative error (σ_s) on the fitted parameters against n_{MAD} for all the band combinations considered

⁶ The choice of the coefficients used to simulate the data does not impact the results, as our procedure is aimed at verifying the ability of our algorithm to recover the coefficients themselves.

⁷ The MAD of a distribution is defined by calculating the absolute deviations from the median and by taking their median value. It defines a symmetric width of the distribution around the median. On the other hand, the DMAD is defined by separating the absolute deviations into values below and above the median distribution and by taking the median of the two subgroups. In this way, the DMAD defines an asymmetrical width of the distribution around the median.

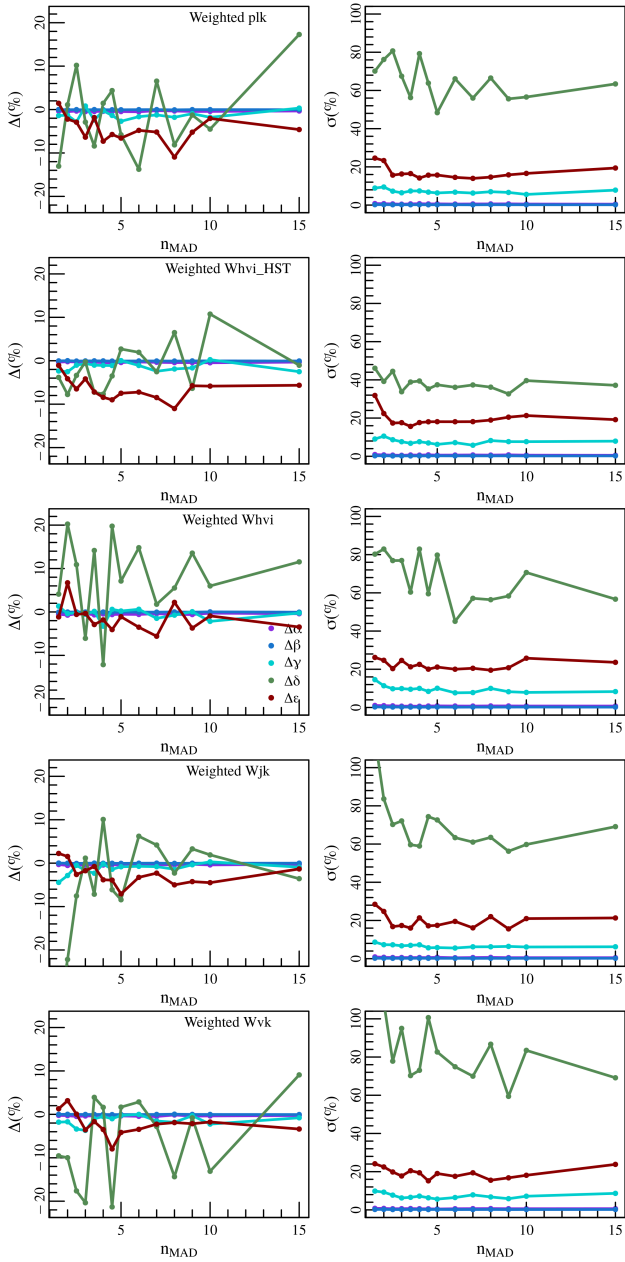


Figure 1. The results obtained by running the weighted Monte Carlo simulations for the $\alpha\beta\gamma\delta\epsilon$ -case. In the left panels the median systematic errors on the fitted parameters are plotted as a function of the n_σ values used for the σ -clipping procedure. The K_s , W_{HVI}^{HST} , W_{HVI} , W_{JK_s} and the W_{VK_s} magnitudes are considered in the various panels from top to bottom, while the different labeled colors represent different parameters (see labels). In the right panels the corresponding relative error (σ s) on the fitted parameters are plotted against n_{MAD} .

in this work. As a further test of the capability of the fitting routine of recovering the correct coefficients, given the difficulty to set the correct weight values in this kind of mathematical problem (Zwolak et al. 2007), we performed a set of 1000 unweighted simulations, whose results are shown in the Fig. A1 for the MAD method.

Looking at Fig. 1 (A1) we can assert that: i) the parameters α and β are recovered with negligible both systematic (left panels) and random errors (right panels), as well as with no evident dependence on the n_σ value; ii) the γ coefficient is not affected by significant system-

atic error, while the random error in many cases, amounts to about 10-15%; iii) the weighted (unweighted) simulations show that the ϵ coefficient is slightly underestimated (overestimated) with respect to the true value by an amount that depends on the band combination, but not larger than 10% and with no evident dependence on the n_σ ; iv) the random error on ϵ always amounts to 20% except for the cases when small n_σ values are used to reject outliers; v) the systematic error on the δ parameter has an highly variable behaviour, with large oscillations indicating both overestimation and underestimation with respect to the true value, but without a clear dependence on the n_σ value and/or on the photometric bands; vi) also the random error on the δ coefficient (right panel) is very large and can amount to more than 100%.

Since there is no clear dependence of the fitting results on the adopted n_σ , except for very small values, we decided to define as systematic and as random errors on the fitted parameters the median of the Δ s and the median of the σ s plotted in Fig. 1 (A1), obtained by excluding the cases with too small n_σ values ($n_\sigma < 2.5$), subject to larger deviations. Moreover, we also calculated the min-max range covered by the quoted Δ s and σ s in order to quantify their variability in the simulations. This effect is shown in Fig. 2 and Fig. 3. Considering that the errors on the α , β and γ are negligible and the parameters are accurately recovered by the fitting routine, the reported figures focus only on the remaining δ and ϵ coefficients.

Figure 2 shows a comparison between the outlier rejection methods. The left panels refer to the systematic errors, while the right panels to the random errors. In each panel, the results for the DMAD are plotted on the abscissa, while those for the MAD are on the ordinate. Moreover, the one-to-one line allows us to assert that both the systematic and random errors on the δ coefficient and those on the ϵ coefficient, are independent of the adopted outlier rejection method. Therefore, to continue our analysis we selected the results obtained from the MAD method and compared the simulations based on the sample of F pulsators with those for the F+10 sample (see Fig. 3, in order to quantify how the inclusion of the 10 sources influences the fit results. Fig. 3 shows that the inclusion of the fundamentalized 10 stars (reported on the abscissa) into the fitted sample allows us to reduce both systematic and random errors for the δ coefficient, and mainly the random errors for what concerns ϵ . On this basis, we decided to focus our analysis on the global F+10 sample.

On the basis of our Monte Carlo simulations, we decided to fit the δ parameter only for the case of the HST bands (orange point in Fig. 3), characterized by a systematic error very close to zero (top-left panel), by a contained variation ($< 10\%$), and by the lowest random error, when compared with the other bands, (top-right panel) amounting to $\approx 40\%$.

On the contrary, our routine allows a quite accurate recovery of the ϵ coefficient, with systematic errors below 10% and random errors around 20% for every band combinations.

The results of this analysis, in combination with those discussed in the subsequent sections, are listed in Table 2. In particular this table contains the values of the systematic and random errors affecting all the fitted coefficients, as derived from the Monte Carlo simulations.

2.3.3 $\alpha\beta\gamma\epsilon$ -case

In this case, we assume that the true PLZ depends on the δ parameter, but we neglect it in the fit to estimate the impact on the other coefficients of the PLZ relations. The results of this second Monte Carlo test are shown in Fig. 4 (A2), which is similar to Fig. 1 (A1), but without the δ coefficient. The main difference with respect to the $\alpha\beta\gamma\delta\epsilon$ -case consists in the larger systematic error on the γ pa-

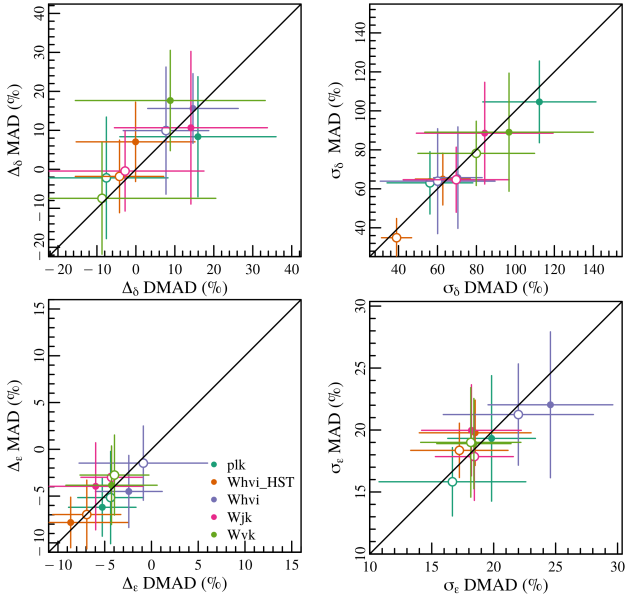


Figure 2. Summary plot of the simulation results for the δ and ϵ coefficients, including all the considered cases. The panels in the left column refer to the systematic errors, while those in the right column are for the random errors. The plotted points are the median values calculated from the simulations as described in the text, while the error bars indicate their range of variation (min-max). Different colors indicate different bands, while empty and filled symbols show the results for F and F+IO cases respectively. Moreover, the one-to-one line is also drawn to facilitate the comparison

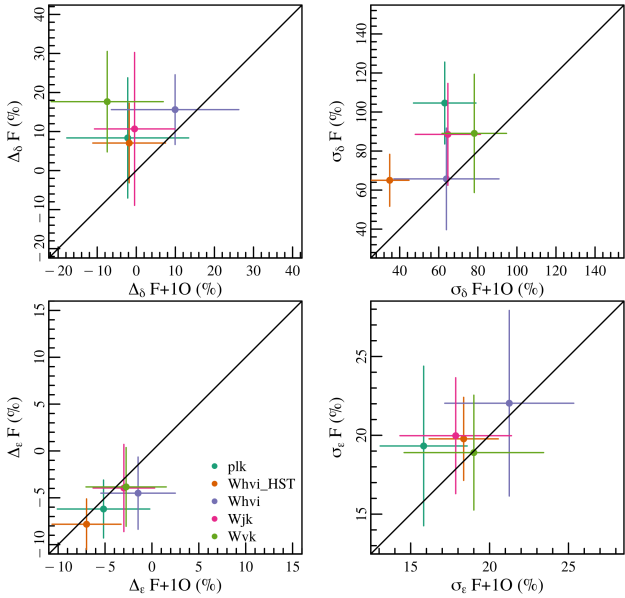


Figure 3. Summary plot of the simulation results for the δ and ϵ coefficients, including all the considered cases. The panels in the left column refer to the systematic errors, while those in the right column are for the random errors. The plotted points are the median values calculated from the simulations as described in the text, while the error bars indicate their range of variation (min-max). Different colors indicate different bands and the one-to-one line is also drawn to facilitate the comparison.

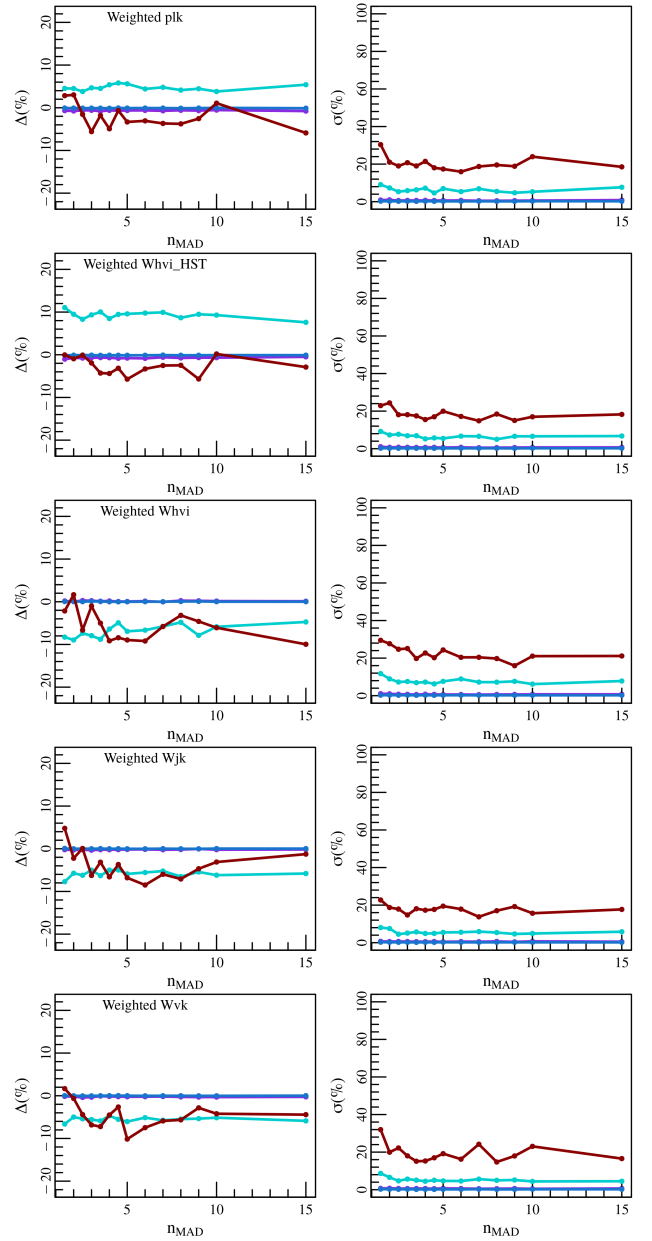


Figure 4. Results obtained by running the Monte Carlo simulations by assuming a 5-parameter PL[FeH]_{true} relation, but neglecting the δ coefficient in the fit. The content of the panels and the meaning of the symbols are the same as in Fig. 1.

parameter, which for some bands (PL_K and PW_{HST}^{HST}) is overestimated up to $\sim 10\%$, and for the remaining bands is underestimated by almost the same amount. We do not show the plot for the unweighted simulations, since it implies similar results.

The results obtained by studying this case are listed in Table 2 and are labeled as $\alpha\beta\gamma\epsilon$ -wt or $\alpha\beta\gamma\epsilon$ -nowt, respectively for the weighted and the unweighted fit.

2.3.4 $\alpha\beta\gamma\epsilon$ -pure -case

The results discussed so far have been obtained by assuming the existence of a dependence on the δ coefficient in Eq. 2. As the significance of this parameter is still uncertain (see e.g. R21), we decided

to perform an additional set of simulations by assuming that this coefficient is zero in the fitted equation (hereafter $\alpha\beta\gamma\epsilon$ -pure case). We verified that the results for this test are similar to those shown in Fig. 4, with the exception of the γ coefficient that is recovered without significant systematic errors.

As for the previously considered cases, the results for this additional set are listed in Table 2 and are labeled as $\alpha\beta\gamma\epsilon$ -pure_{wt} or $\alpha\beta\gamma\epsilon$ -pure_{nowt}, respectively, for the weighted and the unweighted fit.

3 RESULTS

In this section we discuss the coefficients derived from the PLZ/PWZ relations, together with the estimated residual parallax offset. Moreover we describe the application of our fitted relations to derive the LMC distance.

3.1 Implicit fit of the PLZ/PWZ relations

According to the simulations described above, we carried out the ODR procedure by considering all the cases listed in Table 2. We focused our attention on both the weighted and the unweighted fit of the PLZ (PWZ) relations described by eq. 2, where we neglected the δ coefficient, with the exception of the case including the HST band combination. Moreover, we included the fundamentalized IO pulsators in the fitted sample and we did not apply any σ -clipping rejection (see Sect. 2.3). The obtained coefficients were then corrected for the systematic errors found through the simulations and listed in Table 2. In this table we give the rms of the residuals around the fitted ABL relations, even if, for comparison with other estimates, it would be easier, to have PLZ/PWZ dispersion expressed in mag. Anyway, this involves the parallax inversion to calculate the distance and consequently the observed absolute magnitude. As well-known from other studies (Arenou & Luri 1999; Luri et al. 2018; Bailer-Jones et al. 2021), this procedure introduces bias in the distance estimation, that can lead to incorrect results, especially for the sources characterized by a large parallax error ($\sigma_{\varpi}/\varpi > 10\%$). The ABL formalism was introduced to get rid of this problem since the parallax is used linearly by definition. Nevertheless, we tried to give an estimate of the PLZ/PWZ scatter in mag using a non-rigorous procedure. First, for each star, we computed the absolute magnitude using the fitted PLZ/PWZ relationship, by inserting the stars' period and [Fe/H]. Then, we calculated the observed absolute magnitudes for each star by using the apparent dereddened magnitudes (or the Wesenheit magnitudes) and the Gaia parallaxes. Finally, the scatter of the residuals between the observed and computed absolute magnitude is taken as an estimate of the dispersion of the specific PLZ/PWZ relation. We obtained that these dispersions are similar for all the relationships, and of the order of 0.2 mag.

The comparison of the weighted and unweighted coefficients is shown in Fig. 5, where the one-to-one line is drawn together with shaded areas showing three difference levels (in per cent). The parameter best values are in good agreement, with relative differences within 2% for α and β , and below 10% for γ and ϵ . If we include the error bars, the differences between weighted and unweighted results do not rise above 4% for α and β , while for the case of γ and ϵ they can be as large as 40%. The case of the δ coefficient is not considered in the quoted plots because it would be represented by just one point. Anyway, looking at its value in Table 3, the weighted and the unweighted cases differ by 40%, even if they are not significant according to their errors.

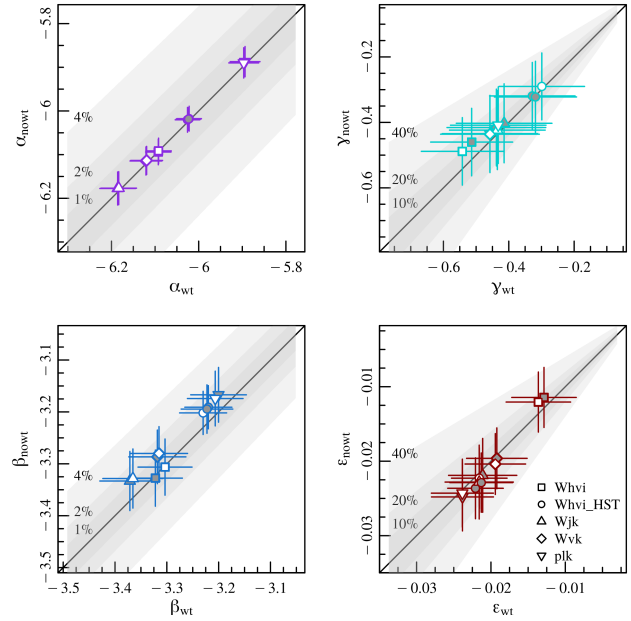


Figure 5. Comparison between the weighted and the unweighted ODR fit α , β , γ and ϵ coefficients listed in Table 3. The weighted values are plotted on the abscissa, while the unweighted are on the ordinates. Different symbols indicate different bands, as labeled in the bottom right panel. For a given band, gray-filled and white-filled points indicate respectively $\alpha\beta\gamma\epsilon$ and $\alpha\beta\gamma\epsilon$ -pure cases. To facilitate the comparison the one-to-one line is also shown, together with a shaded area labeled with three levels of relative difference between the plotted parameters.

The comparison between the $\alpha\beta\gamma\epsilon$ and $\alpha\beta\gamma\epsilon$ -pure cases suggests similar conclusions, with no significant difference between the obtained coefficients (see Fig. 6).

Looking at the values of the statistical error (σ_s) predicted by the Monte Carlo simulations and reported in Table 2, we note that they are systematically smaller than the parameter uncertainties given in Table 3 which lists our final results. This is due to the fact that the latter are obtained by applying the bootstrap technique⁸, while the former descend from Monte Carlo simulations obtained by varying the observational properties within the data errors, as described in the previous section, and are strongly affected by possible overestimation or underestimation of the errors themselves. To be conservative, we will refer to the bootstrap results listed in Table 3.

3.2 The distance of the LMC and the global *Gaia* EDR3 ZP parallax offset

As an application of the derived PLZ (PWZ) relations, we have calculated the LMC distance and compared it with the current accepted geometric value, $\mu_0 = 18.477 \pm 0.026$ mag, derived from the eclipsing binaries (Pietrzyński et al. 2019). Specifically, we applied our relations to the same LMC sample considered by R21. This consists of about 4500 sources and the individual distances have been calculated by using all the considered PLZ relations and by assuming a mean LMC metallicity value [Fe/H] = -0.409 dex ($\sigma = 0.076$ dex)

⁸ The bootstrap simulations are obtained by re-sampling randomly the input data (allowing data point repetitions) and applying the fit to every obtained sample. The distribution of values, obtained for every fitted parameter, is then used to estimate the quoted errors.

| Bands | Δ_α | σ_α | Δ_β | σ_β | Δ_γ | σ_γ | Δ_δ | σ_δ | Δ_ϵ | σ_ϵ | Case |
|---------------------|-----------------|-----------------|----------------|----------------|-----------------|-----------------|-----------------|-----------------|-------------------|-------------------|--|
| Whvi | 0.47 | 0.68 | 0.07 | 0.21 | -6.1 | 7.1 | - | - | 1.9 | 23.0 | $\alpha\beta\gamma\epsilon$ nowt |
| Whvi | -0.17 | 0.65 | 0.02 | 0.21 | -0.27 | 7.5 | - | - | 7.4 | 24.0 | $\alpha\beta\gamma\epsilon$ -pure nowt |
| Whvi | -0.39 | 0.71 | 0.01 | 0.18 | -1.7 | 7.2 | - | - | -0.9 | 20.0 | $\alpha\beta\gamma\epsilon$ -pure wt |
| Whvi | 0.17 | 0.71 | 0.02 | 0.22 | -6.9 | 7.3 | - | - | -6.5 | 22.0 | $\alpha\beta\gamma\epsilon$ wt |
| Whvi _{HST} | -0.10 | 0.63 | 0.05 | 0.18 | 0.26 | 7.1 | 0.54 | 44.0 | 7.2 | 20.0 | $\alpha\beta\gamma\delta\epsilon$ nowt |
| Whvi _{HST} | -0.42 | 0.61 | -0.05 | 0.20 | -1.1 | 7.5 | -1.8 | 35.0 | -7.0 | 18.0 | $\alpha\beta\gamma\delta\epsilon$ wt |
| Whvi _{HST} | -0.49 | 0.72 | -0.01 | 0.20 | 10.0 | 6.3 | - | - | 13.0 | 21.0 | $\alpha\beta\gamma\epsilon$ nowt |
| Whvi _{HST} | -0.15 | 0.63 | 0.04 | 0.20 | 0.00 | 5.4 | - | - | 6.7 | 19.0 | $\alpha\beta\gamma\epsilon$ -pure nowt |
| Whvi _{HST} | -0.38 | 0.68 | -0.04 | 0.18 | -0.40 | 5.7 | - | - | -4.9 | 17.0 | $\alpha\beta\gamma\epsilon$ -pure wt |
| Whvi _{HST} | -0.69 | 0.69 | -0.10 | 0.21 | 9.3 | 6.6 | - | - | -2.6 | 18.0 | $\alpha\beta\gamma\epsilon$ wt |
| Wjk | 0.03 | 0.54 | 0.06 | 0.18 | -5.2 | 4.9 | - | - | 5.0 | 21.0 | $\alpha\beta\gamma\epsilon$ nowt |
| Wjk | -0.12 | 0.59 | 0.05 | 0.19 | -0.29 | 5.4 | - | - | 9.4 | 20.0 | $\alpha\beta\gamma\epsilon$ -pure nowt |
| Wjk | -0.39 | 0.59 | -0.03 | 0.18 | -1.0 | 5.6 | - | - | -3.2 | 19.0 | $\alpha\beta\gamma\epsilon$ -pure wt |
| Wjk | -0.22 | 0.60 | 0.01 | 0.18 | -5.7 | 5.1 | - | - | -5.3 | 17.0 | $\alpha\beta\gamma\epsilon$ wt |
| Wvk | 0.04 | 0.60 | 0.06 | 0.17 | -4.8 | 5.1 | - | - | 6.1 | 20.0 | $\alpha\beta\gamma\epsilon$ nowt |
| Wvk | -0.16 | 0.63 | 0.04 | 0.19 | -0.15 | 5.6 | - | - | 10.0 | 21.0 | $\alpha\beta\gamma\epsilon$ -pure nowt |
| Wvk | -0.36 | 0.61 | -0.03 | 0.18 | -1.3 | 5.3 | - | - | -4.1 | 19.0 | $\alpha\beta\gamma\epsilon$ -pure wt |
| Wvk | -0.27 | 0.63 | -0.01 | 0.20 | -5.5 | 4.9 | - | - | -5.1 | 18.0 | $\alpha\beta\gamma\epsilon$ wt |
| plk | -0.37 | 0.60 | -0.00 | 0.18 | 6.0 | 5.7 | - | - | 9.0 | 21.0 | $\alpha\beta\gamma\epsilon$ nowt |
| plk | -0.15 | 0.60 | 0.04 | 0.19 | -0.31 | 5.3 | - | - | 6.7 | 19.0 | $\alpha\beta\gamma\epsilon$ -pure nowt |
| plk | -0.42 | 0.60 | -0.03 | 0.18 | -1.2 | 5.1 | - | - | -3.1 | 17.0 | $\alpha\beta\gamma\epsilon$ -pure wt |
| plk | -0.62 | 0.63 | -0.08 | 0.20 | 4.6 | 5.7 | - | - | -3.2 | 19.0 | $\alpha\beta\gamma\epsilon$ wt |

Table 2. This table contains the systematic (Δ s) and statistical errors (σ s), expressed in %, used to correct the results of the ODR fit routine for all the considered cases. $\alpha\beta\gamma\delta\epsilon$ is the case where all 4 PLZ/PWZ coefficients are fitted and the parallax offset residual ϵ is estimated simultaneously; $\alpha\beta\gamma\epsilon$ is the case where δ is not fitted but is considered in the PLZ_{true} and the PWZ_{true} relations; finally the $\alpha\beta\gamma\epsilon$ -pure case is where δ is neglected both in the fitting procedure and in the PLZ_{true} and PWZ_{true} relations. The subscripts "nowt" and "wt" refer to a weighted and unweighted fitting. We note that the systematic and random errors for the δ parameter are given only for the Whvi_{HST} case because of too large errors for all the other band combinations, as detailed in the text.

| Bands | N _{dat} | Case | rms _{ABL} | α | β | γ | δ | ϵ | μ_0 |
|---------------------|------------------|--|--------------------|--------------------|--------------------|------------------|------------------|----------------------|--------------------|
| Whvi | 316 | $\alpha\beta\gamma\epsilon$ nowt | 0.017 | -3.328 ± 0.054 | -6.094 ± 0.029 | -0.46 ± 0.10 | - | -0.0114 ± 0.0040 | 18.406 ± 0.044 |
| Whvi | 316 | $\alpha\beta\gamma\epsilon$ -pure nowt | 0.017 | -3.306 ± 0.054 | -6.091 ± 0.029 | -0.49 ± 0.10 | - | -0.0121 ± 0.0040 | 18.401 ± 0.054 |
| Whvi | 316 | $\alpha\beta\gamma\epsilon$ -pure wt | 0.021 | -3.303 ± 0.052 | -6.092 ± 0.029 | -0.54 ± 0.13 | - | -0.0136 ± 0.0043 | 18.381 ± 0.065 |
| Whvi | 316 | $\alpha\beta\gamma\epsilon$ wt | 0.021 | -3.322 ± 0.052 | -6.093 ± 0.029 | -0.51 ± 0.13 | - | -0.0129 ± 0.0043 | 18.385 ± 0.071 |
| Whvi _{HST} | 430 | $\alpha\beta\gamma\delta\epsilon$ nowt | 0.016 | -3.195 ± 0.047 | -6.018 ± 0.026 | -0.32 ± 0.11 | -0.14 ± 0.37 | -0.0229 ± 0.0040 | 18.511 ± 0.078 |
| Whvi _{HST} | 430 | $\alpha\beta\gamma\delta\epsilon$ wt | 0.020 | -3.223 ± 0.050 | -6.023 ± 0.028 | -0.32 ± 0.13 | -0.10 ± 0.38 | -0.0213 ± 0.0042 | 18.499 ± 0.078 |
| Whvi _{HST} | 430 | $\alpha\beta\gamma\epsilon$ nowt | 0.016 | -3.191 ± 0.042 | -6.018 ± 0.028 | -0.32 ± 0.10 | - | -0.0236 ± 0.0041 | 18.489 ± 0.052 |
| Whvi _{HST} | 430 | $\alpha\beta\gamma\epsilon$ -pure nowt | 0.016 | -3.202 ± 0.042 | -6.020 ± 0.028 | -0.29 ± 0.10 | - | -0.0223 ± 0.0041 | 18.499 ± 0.066 |
| Whvi _{HST} | 430 | $\alpha\beta\gamma\epsilon$ -pure wt | 0.020 | -3.230 ± 0.045 | -6.026 ± 0.028 | -0.30 ± 0.13 | - | -0.0216 ± 0.0037 | 18.490 ± 0.055 |
| Whvi _{HST} | 430 | $\alpha\beta\gamma\epsilon$ wt | 0.020 | -3.220 ± 0.045 | -6.022 ± 0.028 | -0.33 ± 0.13 | - | -0.0221 ± 0.0037 | 18.478 ± 0.059 |
| Wjk | 443 | $\alpha\beta\gamma\epsilon$ nowt | 0.016 | -3.333 ± 0.057 | -6.178 ± 0.038 | -0.40 ± 0.12 | - | -0.0219 ± 0.0050 | 18.501 ± 0.068 |
| Wjk | 443 | $\alpha\beta\gamma\epsilon$ -pure nowt | 0.016 | -3.328 ± 0.057 | -6.177 ± 0.038 | -0.42 ± 0.12 | - | -0.0228 ± 0.0050 | 18.494 ± 0.084 |
| Wjk | 443 | $\alpha\beta\gamma\epsilon$ -pure wt | 0.021 | -3.365 ± 0.058 | -6.183 ± 0.041 | -0.44 ± 0.15 | - | -0.0216 ± 0.0046 | 18.477 ± 0.064 |
| Wjk | 443 | $\alpha\beta\gamma\epsilon$ wt | 0.021 | -3.371 ± 0.058 | -6.186 ± 0.041 | -0.41 ± 0.15 | - | -0.0211 ± 0.0046 | 18.485 ± 0.091 |
| Wvk | 430 | $\alpha\beta\gamma\epsilon$ nowt | 0.016 | -3.287 ± 0.052 | -6.115 ± 0.032 | -0.42 ± 0.12 | - | -0.0196 ± 0.0041 | 18.506 ± 0.061 |
| Wvk | 430 | $\alpha\beta\gamma\epsilon$ -pure nowt | 0.016 | -3.280 ± 0.052 | -6.113 ± 0.032 | -0.44 ± 0.12 | - | -0.0204 ± 0.0041 | 18.500 ± 0.061 |
| Wvk | 430 | $\alpha\beta\gamma\epsilon$ -pure wt | 0.021 | -3.315 ± 0.055 | -6.119 ± 0.037 | -0.46 ± 0.15 | - | -0.0194 ± 0.0041 | 18.479 ± 0.072 |
| Wvk | 430 | $\alpha\beta\gamma\epsilon$ wt | 0.021 | -3.318 ± 0.055 | -6.121 ± 0.037 | -0.44 ± 0.15 | - | -0.0192 ± 0.0041 | 18.487 ± 0.070 |
| plk | 443 | $\alpha\beta\gamma\epsilon$ nowt | 0.017 | -3.167 ± 0.053 | -5.887 ± 0.035 | -0.43 ± 0.12 | - | -0.0248 ± 0.0046 | 18.506 ± 0.057 |
| plk | 443 | $\alpha\beta\gamma\epsilon$ -pure nowt | 0.017 | -3.174 ± 0.053 | -5.890 ± 0.035 | -0.41 ± 0.12 | - | -0.0243 ± 0.0046 | 18.516 ± 0.061 |
| plk | 443 | $\alpha\beta\gamma\epsilon$ -pure wt | 0.022 | -3.207 ± 0.054 | -5.897 ± 0.034 | -0.43 ± 0.15 | - | -0.0238 ± 0.0042 | 18.497 ± 0.077 |
| plk | 443 | $\alpha\beta\gamma\epsilon$ wt | 0.022 | -3.200 ± 0.054 | -5.894 ± 0.034 | -0.46 ± 0.15 | - | -0.0238 ± 0.0042 | 18.486 ± 0.061 |

Table 3. This table summarizes the results of the ODR fit: the fitted magnitude is listed in column 1; the number of fitted data points is in column 2; the flag of the fitted case defined in the text is in column 3; the rms of the residuals around the fit is contained in column 4. Note that this quantity is the rms of the ABL function and has therefore the units of the inverse of the square root of a flux (Arenou & Luri 1999); columns 5-9 contain the fitted parameters; the estimated LMC distance for every considered case is contained in column 10.

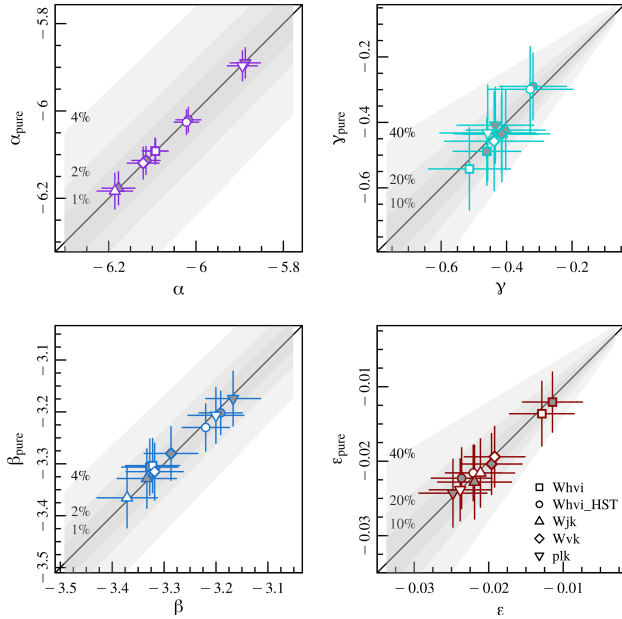


Figure 6. Same as Fig. 5 but for the comparison between the $\alpha\beta\gamma\epsilon$ and $\alpha\beta\gamma\epsilon$ -pure coefficients. In this case, for a given band, gray-filled and white-filled points indicate unweighted and weighted results respectively.

(Romaniello et al. 2022). The LMC distances reported in column 10 of Table 3 are obtained by taking the median of the distribution of the distances of all the selected LMC sources. To calculate the associated error, we have performed 1000 Monte Carlo simulations by varying the PLZ (PWZ) coefficients within their errors and recalculating the LMC arithmetic mean distance every time. The robust standard deviation of the obtained values represents our error.

Figure 7 displays the LMC distance moduli, obtained by using all the fitted PLZ (PWZ) relations, against the parallax offset values, fitted simultaneously through the procedure described above. The main panel of this plot shows that the results from all the PLZ (PWZ) relations are tightly clustered, with the exception of those relative to the HVI band combination, arguably due to some extinction coefficient mismatch. The reported marginal histograms help to visualize the distributions of the plotted data, together with the median values (dashed red lines), adopted as our best estimates of the two parameters (excluding the discrepant HVI combination). They amount respectively to $\epsilon = -22 \mu\text{as}$ ⁹ and $\mu_0^{\text{LMC}} = 18.49 \text{ mag}$, and are also indicated in the main panel by the red triangle. Here the vertical and the horizontal highlighted red regions show the $\pm 1\sigma$ interval of the two distributions equal to $\pm \sim 0.025 \text{ mag}$ and $\pm \sim 3 \mu\text{as}$ respectively for μ_0^{LMC} and ϵ . Anyway, in order to be conservative, the error bars associated to the point, representing our best estimates, are taken equal to the mean uncertainty of the tabulated μ_0^{LMC} and ϵ values, and are equal respectively to $\pm 0.06 \text{ mag}$ and $\pm 4 \mu\text{as}$.

The obtained LMC best distance is in excellent agreement with the accepted geometric value by Pietrzyński et al. (2019) and corresponds to a parallax offset value significantly different from zero,

⁹ In order to better understand the comparison with the literature, discussed in the section below, it is useful here to clarify that the negative correction value found by our fitting procedure indicates that the L21 model returns too large parallaxes.

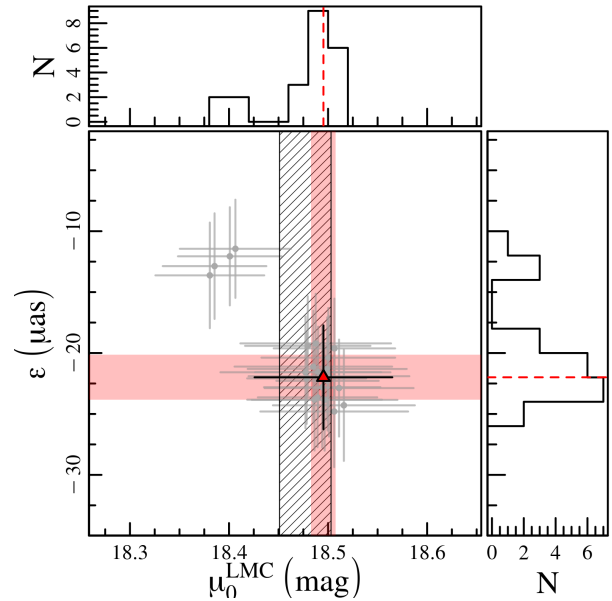


Figure 7. The central panel shows the obtained LMC distance moduli, plotted against the *Gaia* parallax offset values. The grey points represent the results for all the considered cases listed in column 10 of Table 3. Our best values of the two parameters are represented by the red triangle, together with the error bars defined as described in the text. The horizontal and the vertical red regions show the 1σ interval, respectively of the ϵ and μ_0^{LMC} distributions plotted in the two side panels. The skewed-line region encloses the 1σ value around the currently accepted LMC distance 18.477 ± 0.026 obtained by Pietrzyński et al. (2019).

indicating that the L21 recipe applied to the EDR3 parallaxes results into over-corrected values.

4 DISCUSSION

In this section we compare the coefficients of the obtained PLZ/PWZ relations with those obtained from a variety of literature sources.

4.1 Comparison with other PLZ/PWZ coefficients

We have compared the ODR fit results with those obtained recently by R21 by using the same sample of this work but calculated by means of a standard non-linear fitting approach. R21 carried out the PLZ/PWZ relations fit adopting two choices for the global corrections to the individual ZP parallax offsets by L21, namely no global correction at all and a correction of $-14 \pm 6 \mu\text{as}$ (Riess et al. 2021).

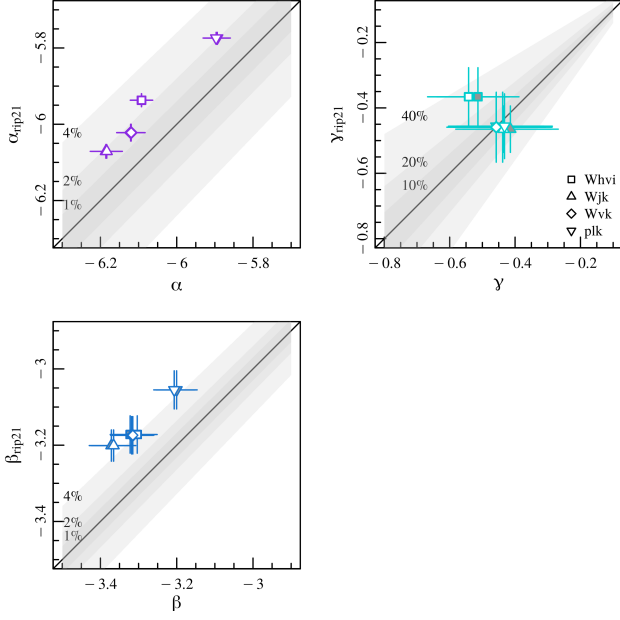


Figure 8. Same as Fig. 5 but it compares the $\alpha\beta\gamma\epsilon$ results with those by R21. Different bands are plotted with different symbols, as labeled in the top right panel. For a give band $\alpha\beta\gamma\epsilon$ and $\alpha\beta\gamma\epsilon$ -pure cases are plotted respectively by white-filled and gray-filled symbols.

The comparison for the first case is shown in Fig. 8 for the parameters α , β and γ . The differences between our results and R21 for the α and β coefficients are within 5%, even if, given the small uncertainties, not consistent with each other at more than 1σ level. Conversely, the γ parameters are consistent with those by R21. The same comparison for the case of global ZP parallax offset as in Riess et al. (2021) is shown in Fig. 9. The α and β coefficients are now consistent within ~ 1 sigma, while the γ coefficients found here are larger (in absolute value), even if consistent within 1σ , compared with R21.

We can use the distance of the LMC to further compare present results with those by R21. They found that the adoption of the global parallax ZP offset has two effects: i) it lowers the absolute value of γ and ii) it provides a distance for the LMC larger than the reference geometric measurement. In this context, the adoption of the global parallax ZP offset found here, namely $-22 \mu\text{as}$, would imply an even larger LMC distance if we had to recalculate the PLZ/PWZ relations by using the standard non-implicit fitting method as in R21. A possible interpretation of this occurrence is the existence of a degeneration (or correlation) between the different coefficients of the fit and the global ZP offset. In the case of the standard non-implicit fitting method, it seems that the largest correlation is with the γ coefficient, while in the case of the implicit method presented here, the α and β values are more affected than γ . This somewhat unexpected behaviour can be tentatively explained taking into account the very different fitting techniques and weighting schemes adopted here and in R21. We expect that the adoption of a larger DCEP sample including e.g. a wider range in metallicity, which should be available in the near future, will allow us to better understand how to break the correlation/degeneracy between the different coefficients of the PLZ/PWZ relations.

We note that, in the C-MetaLL project, we take advantage of high-resolution spectroscopy and multi-band photometry coupled with the *Gaia* parallaxes for a wide sample of Galactic DCEPs to

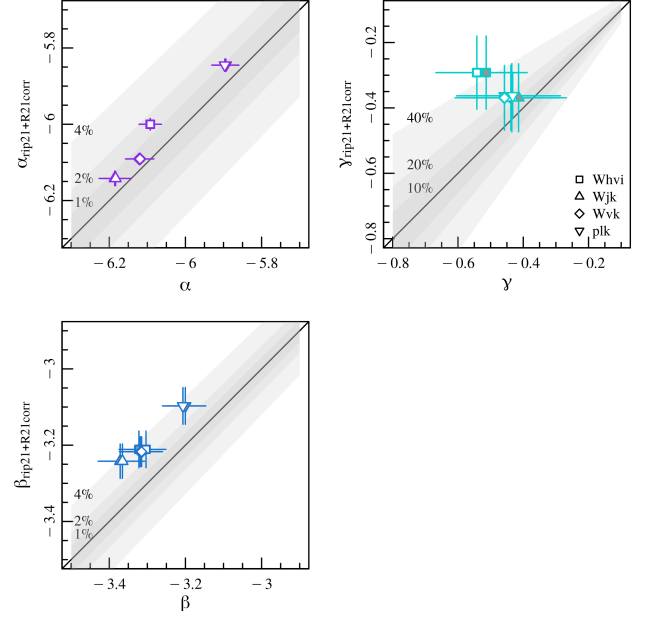


Figure 9. Same as Fig. 5 but it compares the $\alpha\beta\gamma\epsilon$ results with those by R21 including the offset by Riess et al. (2021). Different bands are plotted with different symbols, as labeled in the top right panel. For a give band $\alpha\beta\gamma\epsilon$ and $\alpha\beta\gamma\epsilon$ -pure cases are plotted respectively by white-filled and gray-filled symbols.

fit simultaneously all the coefficients of the PLZ/PWZ relations, thus including the metallicity dependence. On the contrary, in the recent literature the metallicity dependence is tackled by adopting a double-step method: i) The PL/PW relations (no γ in the Eq. 1) are fitted to separate DCEP samples characterized by different mean Z values (e.g. DCEPs belonging to different galaxies); ii) a linear fit is performed to study the dependence of the obtained PL/PW intercepts on the Z mean value of each sample. Albeit this work is mainly aimed at demonstrating the capability of the implicit fit method, in the following we briefly discuss some of the DCEP PLZ/PWZ relations recently presented in the literature.

Gieren et al. (2018) adopted the Baade-Wesselink technique to derive multi-band PL/PW relations ($\text{Mag} = \alpha + \beta(\log P - \log P_0)$) for three samples consisting of 32 Small Magellanic Cloud (SMC), 22 LMC and 14 MW (Milky Way) DCEPs, respectively. According to their results the β coefficient does not change significantly for the three analyzed galaxies, supporting the hypothesis of a metal independent PLZ/PWZ slope. To study the metallicity dependence of the PL/PW zero point, they adopted a mean metallicity value for each considered galaxy and found that the γ coefficient ranges between -0.221 ± 0.053 mag/dex and -0.335 ± 0.059 mag/dex, depending on the photometric bands.

In their recent comprehensive work, Riess et al. (2022) have estimated the metallicity dependence of the PW relation in the HST bands using DCEPs in each geometric anchor galaxy (MW, LMC, SMC, NGC 4258), thus using a method similar to Gieren et al. (2018). In the end they obtained $\gamma = -0.217 \pm 0.046$ mag/dex.

The PLZ/PWZ relations in 15 filters from mid-IR to optical wavelengths were studied by Breuval et al. (2022). They obtained these relations for three samples of DCEPs belonging to MW, LMC and SMC. According to their results there is no strong evidence to reject the hypothesis of a metal independent slope β . Fixing the slope to the LMC value, they studied the intercept dependence on the metallicity.

If we exclude their smallest and largest values, obtained in the *Gaia* bands, their γ coefficient range between -0.20 and -0.33 mag/dex.

The PLZ/PWZ relations were studied also from the theoretical point of view. De Somma et al. (2022) constructed a large set of DCEP pulsational models, characterized by different metallicity values from sub-solar to super-solar, and fitted the PLZ/PWZ relations in the *Gaia*, HST-WFC and Johnson-Cousin photometric systems. They obtained negative γ coefficient, as in the observational studies, albeit with a slightly smaller values.

4.2 Comparison with other ZP parallax offsets

Several authors studied possible residual parallax offset after the application of the correction provided by L21. Different distance tracers, including e.g. quasars, eclipsing binaries, variable stars, open clusters and red clump stars, were used to compare the EDR3 parallaxes to independent distance estimations. According to L21, the correction zero-point for the *Gaia* EDR3 parallaxes is known to be dependent on the ecliptic latitude, the color and the G-band magnitude of the sources. Therefore a direct comparison of our best estimate with those from other authors is not always meaningful.

Fabricius et al. (2021) compared the EDR3 parallaxes with the distances obtained from other external catalogues (see their Tab.1). According to their results, the L21 correction significantly improves the parallax comparison with the exception of the sources belonging the LMC, SMC and two dwarf spheroidal galaxies (Fornax and Sculptor).

Huang et al. (2021) studied the residual offset after L21 correction by using a sample of 65000 red clump stars. According to their results the L21 correction allows to reduce the parallax bias from about $-26\mu\text{as}$, before correction, to $-4\mu\text{as}$.

A slight residual offset is also found by Vasiliev & Baumgardt (2021), who compared the distances of 170 MW globular clusters, collected from the literature, with those released within EDR3. According to their results, the L21 recipe leaves a residual offset equal to $-10\pm 3\mu\text{as}$ in the sense that the corrected parallaxes are larger than the reference distances.

Wang, Yuan, & Huang (2022) used a sample of 0.3 million giant stars with a distance known better than $\sim 10\%$ to find that the official L21 model largely reduces the parallax bias, with a residual offset amounting to $+2.6\mu\text{as}$ ($+2.9\mu\text{as}$) for the five-parameter (six-parameter) solutions, in the sense that the corrected *Gaia* parallaxes are slightly bigger than the reference giant star values.

Similar conclusions were derived by Ren et al. (2021), who used a sample of 0.11 million W-Ursae Major eclipsing binaries (EB) to find a residual parallax offset equal to $+4.2\pm 0.5\mu\text{as}$ ($+4.6\pm 3.7\mu\text{as}$), for the 5-parameters (6-parameters) solutions after the application of the L21 correction.

Using a sample of 158 eclipsing binaries with known bolometric luminosity, Stassun & Torres (2021) found a difference between the L21 corrected *Gaia* parallaxes and those of the reference sample (EDR3^{corr} – EB) equal to $-15\pm 18\mu\text{as}$, even if they consider this difference not statistically significant according to the reported uncertainty. Bhardwaj et al. (2021) used a new calibrated PL relation in the Near Infrared bands to obtain the distances for a sample of Galactic RR Lyrae stars and compared them with those from EDR3 release. They found that the parallaxes obtained by applying the L21 model are over-corrected by $+22\pm 2\mu\text{as}$ in the sense that the L21 parallaxes are too large, in excellent agreement with our findings.

A sample of RR Lyrae variables together with the same implicit fitting procedure of this work, were considered by Gilligan et al. (2021). They calibrated the PLZ relations in the Wide-field Infrared

Survey Explorer (WISE) W1 and W2 bands and simultaneously fitted the *Gaia* EDR3 parallax offset. Their results indicate that the offset value amounts to $+10\pm 7\mu\text{as}$ or $-20\pm 6\mu\text{as}$, respectively by including or excluding the L21 correction.

Using a sample of 74 Galactic DCEPs with Hubble Space Telescope photometry Riess et al. (2021) fitted simultaneously the PWZ and the residual parallax offset, finding that the L21 model over-corrects the raw EDR3 parallaxes by $+14\pm 6\mu\text{as}$ (value already used in this work), in the sense that the corrected values are too big, in agreement with our conclusions and those from the works cited above.

A similar result was reported also by Zinn (2021), who analyzed the asteroseismic data of a sample of red giants observed by Kepler, finding that the corrected EDR3 parallaxes are larger than the reference ones by $+15\pm 5\mu\text{as}$.

In a very recent result by Cruz Reyes & Anderson (2022), the authors estimated the *Gaia* parallax offset by considering both the non-variable open cluster members and the open cluster Cepheids. Their main results are the following: i) the use of non variable cluster stars returns an offset equal to $-4\pm 6\mu\text{as}$, hinting that the L21 model adequately corrects the EDR3 parallaxes in the magnitude range $12.5 < G < 17$ mag; ii) the comparison of the LMC distance, estimated by their calibrated Leawitt laws (obtained in different optical and near-infrared band combinations), with the currently accepted geometric value by Pietrzyński et al. (2019), indicates a residual parallax offset value ranging between $-17\pm 5\mu\text{as}$ and $-22\pm 3\mu\text{as}$, in perfect agreement with the results reported in this work.

To facilitate the comparison of the reported offset values we show Fig. 10 similar to those from Riess et al. (2022) and Li, Casertano, & Riess (2022). The difference between the reference parallaxes and the EDR3 values is on the ordinate, while the G band magnitude for each considered reference sample is on the abscissa. The offset values discussed above are plotted with different colors, while our result is represented by the empty gray star. In the quoted figure, negative (positive) offset values indicate that the true reference parallaxes are smaller (larger) than those obtained after the application of the L21 correction.

5 CONCLUSIONS

In this work we derived simultaneously the coefficients of the DCEPs PLZ (PWZ) relations and the expected offset for the *Gaia* parallaxes. To this aim an implicit form of the fitted relations was adopted, including both the coefficients α , β , γ and δ , characterizing the PLZ (PWZ) relation, together with the parallax offset ϵ . The solution of the implicit fit was achieved by using the ODRPACK95 FORTRAN package, which performs both unweighted fit and weighted fit, taking into account the presence of errors on all the considered variables.

A set of 1000 Monte Carlo simulations, constructed by assuming a fiducial PLZ (PWZ) relation and considering a systematic shift for the *Gaia* parallaxes, was performed in order to test the capability of this tool to recover both reliable coefficient values and the given offset. The presence of possible outlier measurements was also simulated in order to study how the fitting results were affected by these bad points.

As a result of our Monte Carlo experiment, we found that: i) the presence of bad measures does not affect significantly the correct recovery of the PLZ (PWZ) relations; ii) the best results are obtained by enlarging the fitted sample through the inclusion of the fundamentalized IO pulsators; iii) an important finding of our simulations is that the $\alpha\beta\gamma\epsilon$ case yields larger systematics for the γ parameter

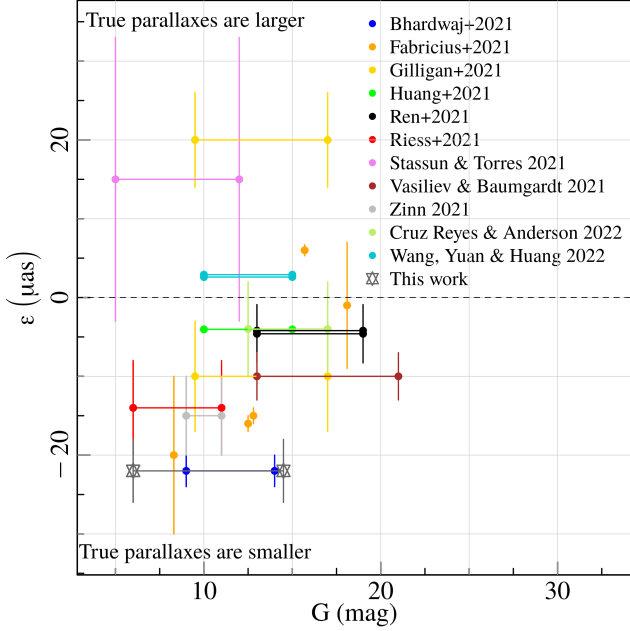


Figure 10. The offset values from the labeled references are plotted as function of the G magnitude range considered in each work. Our estimate is plotted with an empty star. The sign of the ϵ values are such that negative (positive) offset indicate that the true reference parallaxes are smaller (larger) than the EDR3 ones after the L21 correction.

than the $\alpha\beta\gamma\delta\epsilon$ case, while in the $\alpha\beta\gamma\epsilon$ –pure case the dependence on the metallicity is recovered without significant systematics; iv) the determination of metallicity coefficient δ was affected by large errors, both systematic and statistic and we decided not to derive it. This occurrence confirms that the metallicity dependence on the slope is difficult to be constrained, in agreement with our previous results in R21.

We applied the implicit fit technique to a sample of DCEPs already used by R21, obtaining simultaneously the coefficients of a variety of PLZ (PWZ) relations as well as the relative parallax offset to be applied to the L21 corrections. According to our findings, our best estimate of the parallax offset ($\epsilon = -22 \pm 4 \mu\text{as}$) almost cancels the L21 correction, thus indicating that the quoted model over-corrects the EDR3 *Gaia* parallaxes, in agreement with the recent findings by other authors. As a further test, these results, including the parallax offset, were used to calculate the distance to the LMC. The obtained value, $\mu_0 = 18.49 \pm 0.06 \text{ mag}$, is in perfect agreement with the current accepted geometric distance.

This work, albeit not definitive, demonstrated the validity of the implicit fit technique to estimate simultaneously both the PLZ (PWZ) relations and the parallax offset and will be applied to forthcoming works of our group, adopting an improved DCEPs sample possessing precise photometry and accurate chemical abundances.

ACKNOWLEDGEMENTS

The authors thank the Referee for the useful comments that made our work more readable and robust.

This work has made use of data from the European Space Agency (ESA) mission *Gaia* (<https://www.cosmos.esa.int/gaia>), processed by the *Gaia* Data Processing and Analysis Consortium (DPAC, <https://www.cosmos.esa.int/web/gaia/dpac/>

consortium). Funding for the DPAC has been provided by national institutions, in particular the institutions participating in the *Gaia* Multilateral Agreement. In particular, the Italian participation in DPAC has been supported by Istituto Nazionale di Astrofisica (INAF) and the Agenzia Spaziale Italiana (ASI) through grants I/037/08/0, I/058/10/0, 2014-025-R.0, and 2014-025-R.1.2015 to INAF (PIM.G. Lattanzi).

DATA AVAILABILITY

All the data used in this work have already been published and can be found in Ripepi et al. (2021), and references therein).

REFERENCES

- Anderson R. I., Saio H., Ekström S., Georgy C., Meynet G., 2016, *A&A*, 591, A8. doi:10.1051/0004-6361/201528031
- Arenou F., Luri X., 1999, *ASPC*, 167, 13
- Arenou F., Luri X., Babusiaux C., Fabricius C., Helmi A., Muraveva T., Robin A. C., et al., 2018, *A&A*, 616, A17. doi:10.1051/0004-6361/201833234
- Bailer-Jones C. A. L., Rybizki J., Fouesneau M., Demleitner M., Andrae R., 2021, *AJ*, 161, 147. doi:10.3847/1538-3881/abd806
- Bhardwaj A., Rejkuba M., de Grijs R., Yang S.-C., Herczeg G. J., Marconi M., Singh H. P., et al., 2021, *ApJ*, 909, 200. doi:10.3847/1538-4357/abdf48
- Boggs, P. T., R. H. Byrd, J. R. Donaldson, and R. B. Schnabel (1989), “Algorithm 676 — ODRPACK: Software for Weighted Orthogonal Distance Regression,” *ACM Trans. Math. Software*, 15(4):348–364
- Breival L., Kervella P., Anderson R. I., Riess A. G., Arenou F., Trahin B., Mérand A., et al., 2020, *A&A*, 643, A115. doi:10.1051/0004-6361/202038633
- Breival L., Kervella P., Wielgórski P., Gieren W., Graczyk D., Trahin B., Pietrzyński G., et al., 2021, *ApJ*, 913, 38. doi:10.3847/1538-4357/abf0ae
- Breival L., Riess A. G., Kervella P., Anderson R. I., Romaniello M., 2022, *ApJ*, 939, 89. doi:10.3847/1538-4357/ac97e2
- Caputo F., Marconi M., Musella I., 2000, *A&A*, 354, 610
- Cardelli J. A., Clayton G. C., Mathis J. S., 1989, *ApJ*, 345, 245. doi:10.1086/167900
- Cruz Reyes M., Anderson R. I., 2022, arXiv, arXiv:2208.09403
- De Somma G., Marconi M., Molinaro R., Ripepi V., Leccia S., Musella I., 2022, *ApJS*, 262, 25. doi:10.3847/1538-4365/ac7f3b
- Fabricius C., Luri X., Arenou F., Babusiaux C., Helmi A., Muraveva T., Reylé C., et al., 2021, *A&A*, 649, A5. doi:10.1051/0004-6361/202039834
- Feast, M. W. & Catchpole, R. M. 1997, *MNRAS*, 286, L1
- Gaia* Collaboration, 2017, *A&A*, 605, A79
- Gaia* Collaboration, Prusti T., de Bruijne J. H. J., Brown A. G. A., Vallenari A., Babusiaux C., Bailer-Jones C. A. L., et al., 2016, *A&A*, 595, A1. doi:10.1051/0004-6361/201629272
- Gaia* Collaboration, Brown A. G. A., Vallenari A., Prusti T., de Bruijne J. H. J., Babusiaux C., Bailer-Jones C. A. L., et al., 2018, *A&A*, 616, A1. doi:10.1051/0004-6361/201833051
- Gaia* Collaboration, Brown A. G. A., Vallenari A., Prusti T., de Bruijne J. H. J., Babusiaux C., Biermann M., et al., 2021, *A&A*, 649, A1. doi:10.1051/0004-6361/202039657
- Genovali K., Lemasle B., Bono G., Romaniello M., Fabrizio M., Ferraro I., Iannicola G., et al., 2014, *A&A*, 566, A37. doi:10.1051/0004-6361/201323198
- Gieren W., Storm J., Konorski P., Górski M., Pilecki B., Thompson I., Pietrzyński G., et al., 2018, *A&A*, 620, A99. doi:10.1051/0004-6361/201833263
- Gilligan C. K., Chaboyer B., Marengo M., Mullen J. P., Bono G., Braga V. F., Crestani J., et al., 2021, *MNRAS*, 503, 4719. doi:10.1093/mnras/stab857
- Groenewegen M. A. T., 2018, *A&A*, 619, A8. doi:10.1051/0004-6361/201833478
- Huang Y., Yuan H., Beers T. C., Zhang H., 2021, *ApJL*, 910, L5. doi:10.3847/2041-8213/abe69a

- L. Inno et al 2016 ApJ 832 176
- Layden A. C., Tiede G. P., Chaboyer B., Bunner C., Smitka M. T., 2019, AJ, 158, 105. doi:10.3847/1538-3881/ab2e10
- Leavitt H. S., Pickering E. C., 1912, HarCi, 173
- Levenberg, K. 1944, Quarterly of Applied Mathematics, 2, 164
- Leung H. W., Bovy J., 2019, MNRAS, 489, 2079. doi:10.1093/mnras/stz2245
- Li S., Casertano S., Riess A. G., 2022, ApJ, 939, 96. doi:10.3847/1538-4357/ac7559
- Lindgren L., Hernández J., Bombrun A., Klioner S., Bastian U., Ramos-Lerate M., de Torres A., et al., 2018, A&A, 616, A2. doi:10.1051/0004-6361/201832727
- Lindgren L., Bastian U., Biermann M., Bombrun A., de Torres A., Gerlach E., Geyer R., et al., 2021, A&A, 649, A4. doi:10.1051/0004-6361/202039653
- Luri X., Brown A. G. A., Sarro L. M., Arenou F., Bailer-Jones C. A. L., Castroginar A., de Bruijne J., et al., 2018, A&A, 616, A9. doi:10.1051/0004-6361/201832964
- Lutz T. E., Kelker D. H., 1973, PASP, 85, 573. doi:10.1086/129506
- Madore B. F., 1982, ApJ, 253, 575
- Marconi, M., Molinaro, R., Ripepi, V., et al. 2021, MNRAS, 500, 5009
- Marquardt, D. W. 1963, SIAM J. Appl. Math., 11, 431
- Ngeow C.-C., 2012, ApJ, 747, 50. doi:10.1088/0004-637X/747/1/50
- Pietrzyński G., Graczyk D., Gellenne A., Gieren W., Thompson I. B., Pilecki B., Karczmarek P., et al., 2019, Natur, 567, 200. doi:10.1038/s41586-019-0999-4
- Planck Collaboration, Aghanim N., Akrami Y., Ashdown M., Aumont J., Bacigalupi C., Ballardini M., et al., 2020, A&A, 641, A6. doi:10.1051/0004-6361/201833910
- Ren F., Chen X., Zhang H., de Grijs R., Deng L., Huang Y., 2021, ApJL, 911, L20. doi:10.3847/2041-8213/abf359
- Ripepi V., Molinaro R., Musella I., Marconi M., Leccia S., Eyer L., 2019, A&A, 625, A14. doi:10.1051/0004-6361/201834506
- Ripepi V., Catanzaro G., Molinaro R., Marconi M., Clementini G., Cusano F., De Somma G., et al., 2020, A&A, 642, A230. doi:10.1051/0004-6361/202038714
- Ripepi V., Catanzaro G., Molinaro R., Gatto M., De Somma G., Marconi M., Romaniello M., et al., 2021, MNRAS, 508, 4047. doi:10.1093/mnras/stab2460
- Ripepi V., Catanzaro G., Clementini G., De Somma G., Drimmel R., Leccia S., Marconi M., et al., 2022, A&A, 659, A167. doi:10.1051/0004-6361/202142649
- Riess A. G., Macri L. M., Hoffmann S. L., Scolnic D., Casertano S., Filippenko A. V., Tucker B. E., et al., 2016, ApJ, 826, 56
- Riess A. G., Casertano S., Yuan W., Bowers J. B., Macri L., Zinn J. C., Scolnic D., 2021, ApJL, 908, L6. doi:10.3847/2041-8213/abdbaf
- Riess A. G., Yuan W., Macri L. M., Scolnic D., Brout D., Casertano S., Jones D. O., et al., 2022, ApJL, 934, L7. doi:10.3847/2041-8213/ac5c5b
- Romaniello M., Riess A., Mancino S., Anderson R. I., Freudling W., Kudritzki R.-P., Macri L., et al., 2022, A&A, 658, A29. doi:10.1051/0004-6361/202142441
- Stassun K. G., Torres G., 2021, ApJL, 907, L33. doi:10.3847/2041-8213/abdaad
- Trentin E., Ripepi V., Catanzaro G., Storm J., Marconi M., De Somma G., Testa V., et al., 2022, arXiv, arXiv:2209.03792
- van Leeuwen F., Feast M. W., Whitelock P. A., Laney C. D., 2007, MNRAS, 379, 723. doi:10.1111/j.1365-2966.2007.11972.x
- Vasiliev E., Baumgardt H., 2021, MNRAS, 505, 5978. doi:10.1093/mnras/stab1475
- Wang C., Yuan H., Huang Y., 2022, AJ, 163, 149. doi:10.3847/1538-3881/ac4dec
- Zwolak, J. W., Boggs, P. T., & Watson, L. T. 2007, ACM Transactions on Mathematical Software, 33, 27
- Zinn J. C., 2021, AJ, 161, 214. doi:10.3847/1538-3881/abe936

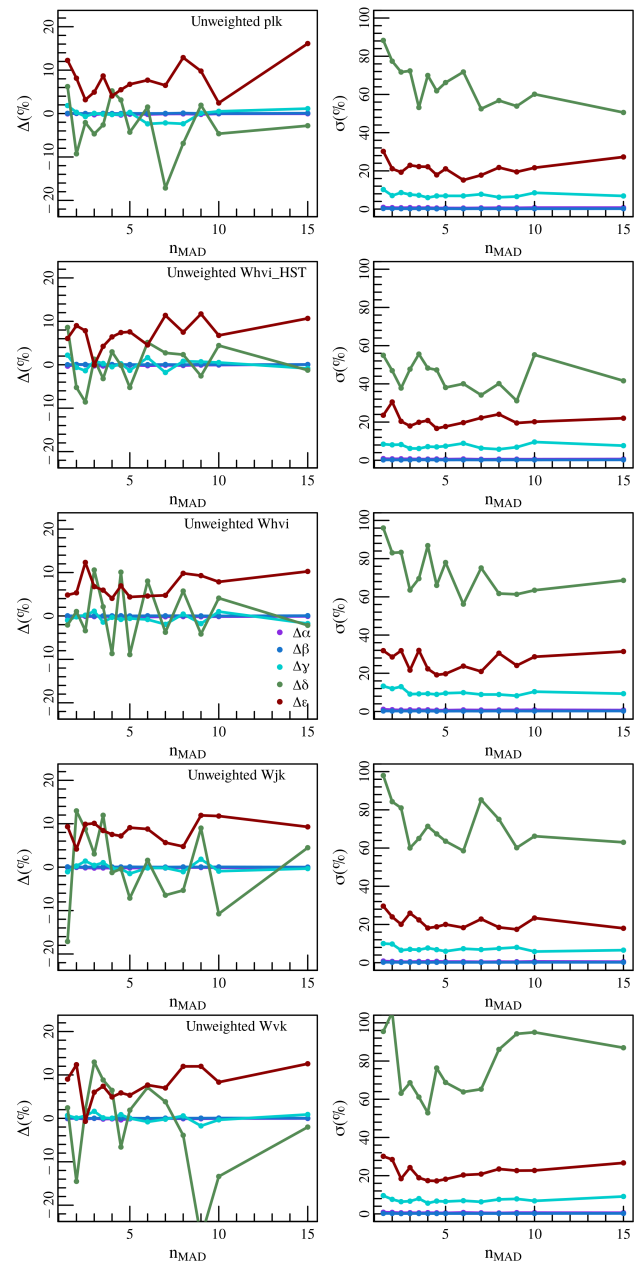


Figure A1. This figure shows the results obtained by running the Monte Carlo simulations by assuming a 5-parameters PL[FeH] relation and performing an unweighted fit. The meaning of the panels and of the symbols are the same as in the Fig. 1.

APPENDIX A: MONTE CARLO SIMULATIONS

A1 The 5-parameter model: unweighted fit of α , β , γ , δ and ϵ

A2 The 4-parameter model: neglecting δ

This paper has been typeset from a $\text{\TeX}/\text{\LaTeX}$ file prepared by the author.

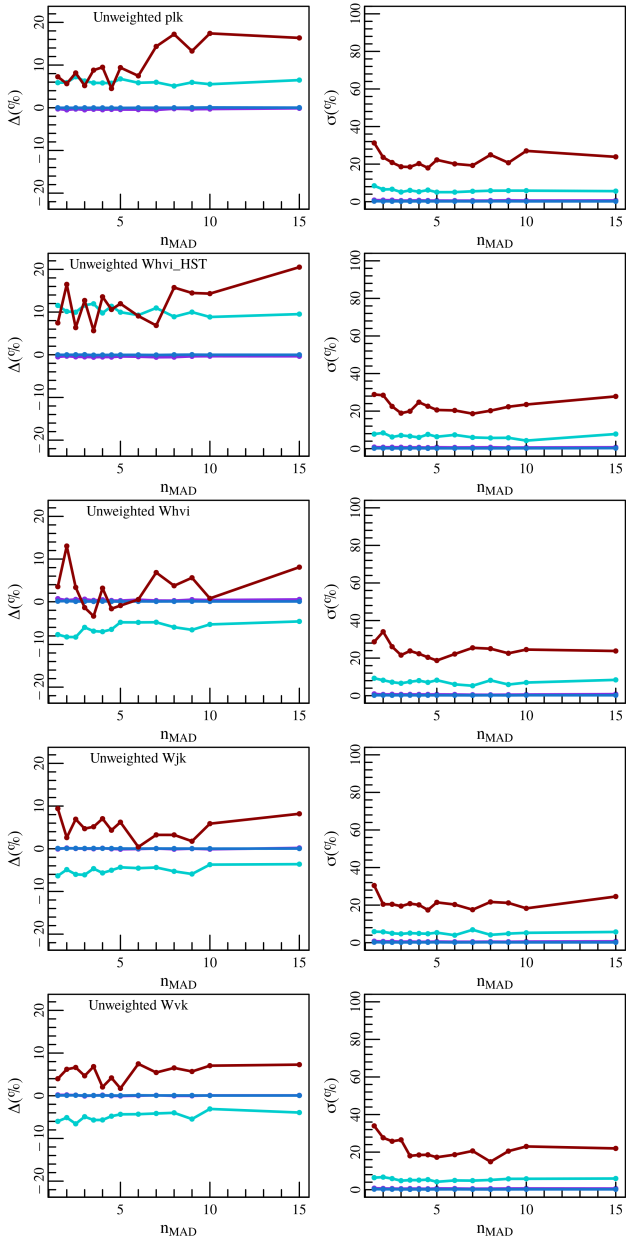


Figure A2. This figure is the same as A1 but obtained by neglecting the dependence on δ in both the true and the fitted PLZ (PWZ) relations.